Infrared Organic Photodetectors Employing Ultralow Bandgap Polymer and Non-Fullerene Acceptors for Biometric Monitoring

Polina Jacoutot, Alberto D. Scaccabarozzi, Tianyi Zhang, Zhuoran Qiao, Filip Aniés, Marios Neophytou, Helen Bristow, Rhea Kumar, Maximilian Moser, Alkmini D. Nega, Andriana Schiza, Antonia Dimitrakopoulou-Strauss, Vasilis G. Gregoriou, Thomas D. Anthopoulos, Martin Heeney, Iain McCulloch, Artem A. Bakulin, Christos L. Chochos, and Nicola Gasparini*

Recent efforts in the field of organic photodetectors (OPD) have been focused on extending broadband detection into the near-infrared (NIR) region. Here, two blends of an ultralow bandgap push–pull polymer TQ-T combined with state-of-the-art non-fullerene acceptors, IEICO-4F and Y6, are compared to obtain OPDs for sensing in the NIR beyond 1100 nm, which is the cut off for benchmark Si photodiodes. It is observed that the TQ-T:IEICO-4F device has a superior IR responsivity (0.03 AW^{-1} at 1200 nm and −2 V bias) and can detect infrared light up to 1800 nm, while the TQ-T:Y6 blend shows a lower responsivity of 0.01 AW^{-1}. Device physics analyses are tied with spectroscopic and morphological studies to link the superior performance of TQ-T:IEICO-4F OPD to its faster charge separation as well as more favorable donor–acceptor domains mixing. In the polymer blend with Y6, the formation of large agglomerates that exceed the exciton diffusion length, which leads to high charge recombination, is observed. An application of these devices as biometric sensors for real-time heart rate monitoring via photoplethysmography, utilizing infrared light, is demonstrated.

1. Introduction

The optical sensor market is currently going through an intensive growth phase to fulfil the requirement in detectors for imaging, smartphones, and automotive vehicles, as well as for applications in biomedicine,[1] optical communication,[2] security, and environmental monitoring. Organic electronic technology involving carbon-based semiconductor materials has many desirable features compared to its inorganic counterpart including room-temperature processing from solution and reduced manufacturing costs while delivering large areas of lightweight, flexible devices with strong light absorption and optical and electronic tuneability.[3–7]

Emerging designs for biological imaging operate within the second

P. Jacoutot, T. Zhang, Z. Qiao, F. Aniés, R. Kumar, M. Heeney,
A. A. Bakulin, N. Gasparini
Department of Chemistry and Centre for Processable Electronics
Imperial College London
London W12 0BZ, UK
E-mail: n.gasparini@imperial.ac.uk

A. D. Scaccabarozzi, T. D. Anthopoulos, I. McCulloch
King Abdullah University of Science and Technology (KAUST)
KAUST Solar Center (KSC)
Thuwal 23955, Saudi Arabia

The ORCID identification number(s) for the author(s) of this article can be found under https://doi.org/10.1002/smll.202200580.

M. Neophytou, H. Bristow, M. Moser, I. McCulloch
Department of Chemistry
Chemistry Research Laboratory
University of Oxford
Oxford OX1 3TA, UK

A. D. Nega, A. Dimitrakopoulou-Strauss
Clinical Cooperation Unit Nuclear Medicine
German Cancer Research Center
69120 Heidelberg, Germany

A. Schiza, C. L. Chochos
Institute of Chemical Biology
National Hellenic Research Foundation
48 Vassileos Constantinou Avenue, Athens 11635, Greece

V. G. Gregoriou, C. L. Chochos
Advent Technologies SA
Stadiou Street, Platani, Rio, Patras 26504, Greece

V. G. Gregoriou
National Hellenic Research Foundation
48 Vassileos Constantinou Avenue, Athens 11635, Greece

(NIR-II: 1000–1300 nm) and third (NIR-III: 1550–1870 nm) biological windows, which offer deeper tissue penetration, improved image contrast, and reduced photobleaching.[1,8,9] This makes organic devices that can detect those spectral regions while delivering conformal coverage, biocompatibility, and lack of cooling requirements, a preferred choice for wearable health monitors.[10–12] Between the pool of organic semiconductor devices, organic photodetectors (OPDs) based on near-infrared (NIR) materials have the potential to outperform commercially available sensors for cardiac recordings as well as for blood oximeters.[4,13,14] This latter feature is of utmost importance for health monitoring, for example, SARS-CoV-2 detection.[15,16] However, the wide bandgaps of solution-processible molecular semiconductors present challenges in realizing infrared detection above wavelengths of 1 µm. Many advances in the design of infrared-sensing materials were achieved during the development of bulk heterojunction (BHJ) organic photovoltaics (OPV) to enhance their solar light harvesting and power conversion efficiencies.[17–21] This has greatly impacted the OPD field, as OPDs share certain working principles with OPV, and can benefit from the rapid increase in the available array of low-bandgap materials.[2,22]

The main synthetic strategy to lower the bandgap and tune the electronic levels of conjugated polymers for OPV/OPD applications, involves the stabilization of the semiconductors' quinoid resonance form, the use of alternating donor and acceptor units, or a combination of both methods.[23–25] One of the pioneering works in this field used a thiadiazoloquinoxaline unit to lower the polymer bandgap to 1 eV and push its absorption tail up to 1200 nm.[26] However, with these NIR absorbing polymers, low open-circuit voltages (V_{oc}) were obtained for polymer:fullerene blends in OPV. This is due to the small difference between the highest occupied molecular orbital (HOMO) of the donor and the lowest unoccupied molecular orbital (LUMO) of the acceptor.[25] Alternatively, low bandgap non-fullerene acceptors (NFAs) can be used to address fullerene's limitations, and provide more tunability in the energy offsets between the donor and acceptor.[27,28] The renaissance of NFAs was first driven by the OPV field in an effort to minimize manufacturing costs and voltage losses via energy level tuning. Small molecule acceptors also became popular in OPD research as lower-cost materials with tunable absorptions.[19,29–31] Still, to this day, the choice of organic NIR devices with detection up to 1400 nm remains scarce with only a few studies reporting detection up to 1600 nm (Table S1, Supporting Information).[13]

Along with new materials synthesis, various device engineering solutions have successfully pushed the detectivity further into the infrared region.[32] For example, optically thick cavities have enabled truly narrowband detection in the NIR region using sub-bandgap photons through charge collection narrowing.[33] Alternatively, harvesting sub-bandgap absorption of charge-transfer states has been used for NIR detection, as recently demonstrated for a variety of fullerene-based OPDs.[34–37] Nonetheless, these methods also suffer from low external quantum efficiencies (EQEs), compared to the much more abundant visible detector library.[38]

Until very recently, no theoretical limit for specific detectivity (D^*) has been identified for OPDs and the longest achievable detection wavelength is still unknown.[39] The calculated detectivity limits for 1500 and 2000 nm have been estimated at 10^{12} and 10^{10} Jones, respectively, as a result of non-radiative dark saturation current that is a limiting factor at longer wavelengths.[39]

In this work, we demonstrate two NIR organic photodetectors based on donor–acceptor (D-A) bulk heterojunction blends, using an ultralow bandgap polymer (TQ-T) and NFAs with a spectral responsivity up to 1800 nm. TQ-T belongs to the class of D-A type conjugated polymers and comprises a para alkoxyphenyl substituted thiadiazoloquinoxaline (TQ) as highly electron-deficient moiety and thiophene as a high electron-rich unit. This results in an ultralow bandgap of <0.7 eV.[40] We investigated the organic photodetector performance of two blends of the polymer with the established non-fullerene acceptors IEICO-4F[41] and Y6[42] and provide spectroscopic evidence to explain the superior responsivity and specific detectivity of the IEICO-4F-based device in the infrared window. In particular, we found that the finer microstructure in TQ-T:IEICO-4F blends leads to faster charge transfer and lower charge recombination, resulting in a dark current of 8.4×10^{-3} mA cm^{-2} and D^* of 10^{10} Jones in the NIR at −2 V. Furthermore, we provide a scope for biometric applications for this device by demonstrating real-time contactless heart rate monitoring with high signal resolution in the infrared.

2. Results and Discussion

The photoactive layer of the NIR-OPD devices comprises the ultra-narrow bandgap (E_g) donor polymer TQ-T, previously reported for ambipolar organic field-effect transistors,[40] and either one of the small molecule non-fullerene acceptors IEICO-4F and Y6. The chemical structures, their absorption profiles, and energy levels are depicted in **Figure 1**. The HOMO levels were obtained from photoelectron spectroscopy in air measurements (Figure S1, Supporting Information), while LUMO levels were calculated as LUMO = HOMO + E_g. We selected IEICO-4F and Y6 as electron acceptors for their complementary absorption (Figure 1b) with TQ-T and energy alignments (Figure 1c) that allow sufficient energetic offset for exciton separation. We fabricated OPD devices based on an inverted structure consisting of indium tin oxide (ITO)/ZnO/Active layer/MoO$_x$/Ag (Figure 1d), with the photoactive layer spin-coated in N$_2$-controlled environment. We first analyzed the photodetection ability of TQ-T:IEICO-4F and TQ-T:Y6 blends by measuring device current density–voltage (J–V) characteristics under 1 sun illumination (AM1.5G) and dark conditions (**Figure 2**a). For real-world applications, low dark currents (J_d) at −2 V are desired in order to maximize the ratio between the light current (J_L) and J_d. TQ-T:IEICO-4F and TQ-T:Y6 delivered J_d at −2 V of 8.4×10^{-3} mA cm^{-2} and 4.3×10^{-2} mA cm^{-2}, respectively. As will be described later, the lower J_d in TQ-T:IEICO-4F is related to a superior charge extraction and reduced charge recombination than Y6-based blends. It is worth mentioning that the relatively high J_d reported for these ultralow E_g blends can be related to a non-ohmic contact between the HOMO of the donor polymer and the hole-transporting layer used and the intrinsic recombination losses associated with the NIR-based OPD.[39]

For efficient detection of light, in addition to low J_d, high light-to-current conversion is required. For this reason, we

**ADVANCED
SCIENCE NEWS**

www.advancedsciencenews.com

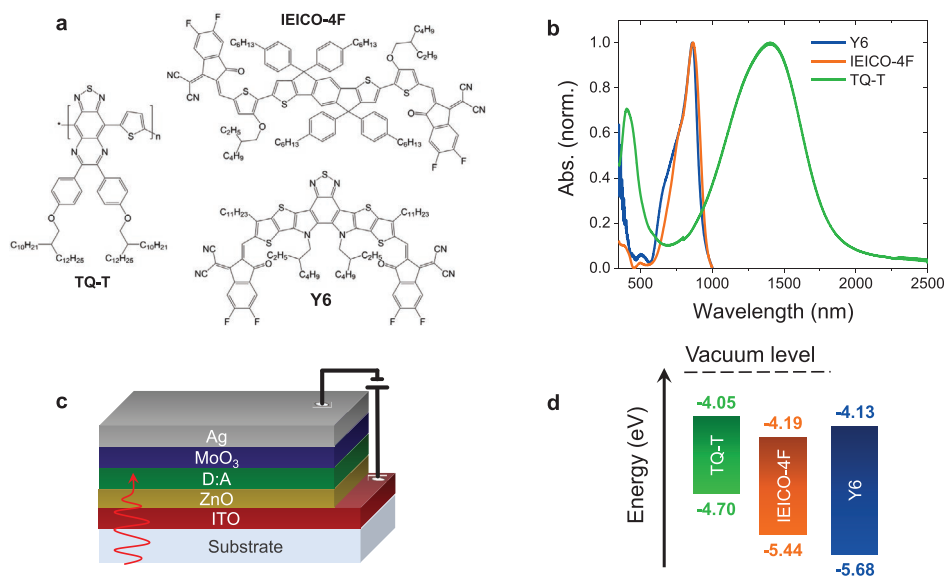**NANO · MICRO
small**

www.small-journal.com

Figure 1. a) Chemical structures of TQ-T, IEICO-4F, and Y6; b) normalized absorbance of the neat materials; c) molecular energy levels of the materials; d) schematic of the BHJ donor-acceptor device structure with inverted architecture.

measured the responsivity (*R*) of TQ-T-based blends. Figure 2b shows the *R* plots of TQ-T:IEICO-4F and TQ-T:Y6 blends at −2 V. The external quantum efficiency plots are reported in Figure S2 (Supporting Information). Interestingly, both devices exhibited similar *R* values of 0.09–0.11 A W^{-1} at 900 nm, which reflects the similar light conversion associated with the NFAs used. Notably, the absorption of the NFA is stronger than the polymer in both 1:1 blends (Figures S3 and S4, Supporting Information) due to the high optical constants of the NFAs as observed by Meredith and co-workers.[29] This efficient harvesting in the acceptor region translates to higher responsivity compared to the donor region.

In the polymer absorption region above 1000 nm, we observed a broad photoresponse in 1000–1800 nm range for TQ-T:IEICO-4F with a maximum *R* of 0.03 A W^{-1} at 1200 nm, while TQ-T:Y6 blends showed lower *R* values (0.01 A W^{-1}) in the NIR region. The different ability to convert infrared light into the current is not related to the energetic driving force for exciton dissociation since a large offset between the frontier energy alignment is present in the two blends. As described later, the greater *R* values in TQ-T:IEICO-4F blends are due to a combination of finer microstructure and reduced charge recombination.

One of the key metrics to compare different photodetector technologies is the specific detectivity. *D** takes into account both the signal stability and the photodetection ability, identified by the noise current (*i$_n$*) and responsivity, respectively, as described by Equation (1).

$$D^* = \frac{\sqrt{A \Delta f}\, R}{i_n} \quad (1)$$

where *A* is the photodetector active area and Δ*f* is the measurement system bandwidth. The noise current (*i$_n$*) is calculated according to Equation (2), where *q* is the elementary charge, *i$_d$* is the dark current, *k* is the Boltzmann constant, *T* is the temperature, and *R*$_{shunt}$ is the shunt resistance.

$$(i_n)^2 = \left(2qi_d + \frac{4kT}{R_{shunt}} \right) \quad (2)$$

Figure S5 (Supporting Information) shows the fast Fourier transform of the dark current. The noise floor was reached for both OPDs at a frequency as low as 0.1 Hz, suggesting that for frequencies above 0.1 Hz the flicker noise is negligible. Figure 2c shows the *D** as a function of wavelength at −2 V for TQ-T:IEICO-4F and TQ-T:Y6 devices. Due to the extended responsivity and lower *i$_n$*, TQ-T:IEICO-4F OPD devices delivered *D** of 10^9–10^{10} Jones in the UV–Vis–NIR range, while TQ-T:Y6 shows *D** of 10^7–10^8 Jones across the NIR region (1000–1800 nm). The *D** values obtained for TQ-T:IEICO-4F blends are promising for applications that require NIR detection, i.e., night cameras and oximeter sensors. Considering only the dark current contribution to the output signal of OPDs has been observed to lead to significant overestimations in noise equivalent power and *D**.[43] In fact, the *D** values determined using this approximation are overestimated, with *D** values approaching 10^{11} Jones being calculated for the TQ-T:IEICO-4F-based OPD. These values for *D** are presented in Figure S6 (Supporting Information).

These applications require, in addition to efficient light-to-current conversion, high contrast and fast response speed. For this reason, we measured the light dynamic range (LDR) of the devices, defined as the ratio between the photocurrent (*J*$_{ph}$ = *J$_l$* − *J$_d$*, where *J$_d$* and *J$_l$* are the current densities under light and dark conditions, respectively) at high (*j*$_{max}$) and low (*j*$_{min}$) light intensities, according to LDR = 20log (*j*$_{max}$/*j*$_{min}$), see Figure S7 (Supporting Information).

Figure 3a depicts the LDR plots for IEICO-4F and Y6-based blends extracted under AM1.5G illumination. A linear trend of *J*$_{ph}$ versus light intensity is observed down to illumination levels of 0.1 mW cm^{-2} for TQ-T:IEICO-4F and 1 mW cm^{-2} for TQ-T:Y6 OPD devices. We then calculated LDR values at −2 V of 45.8 dB and 35.7 dB for TQ-T:IEICO-4F and TQ-T:Y6, respectively, in
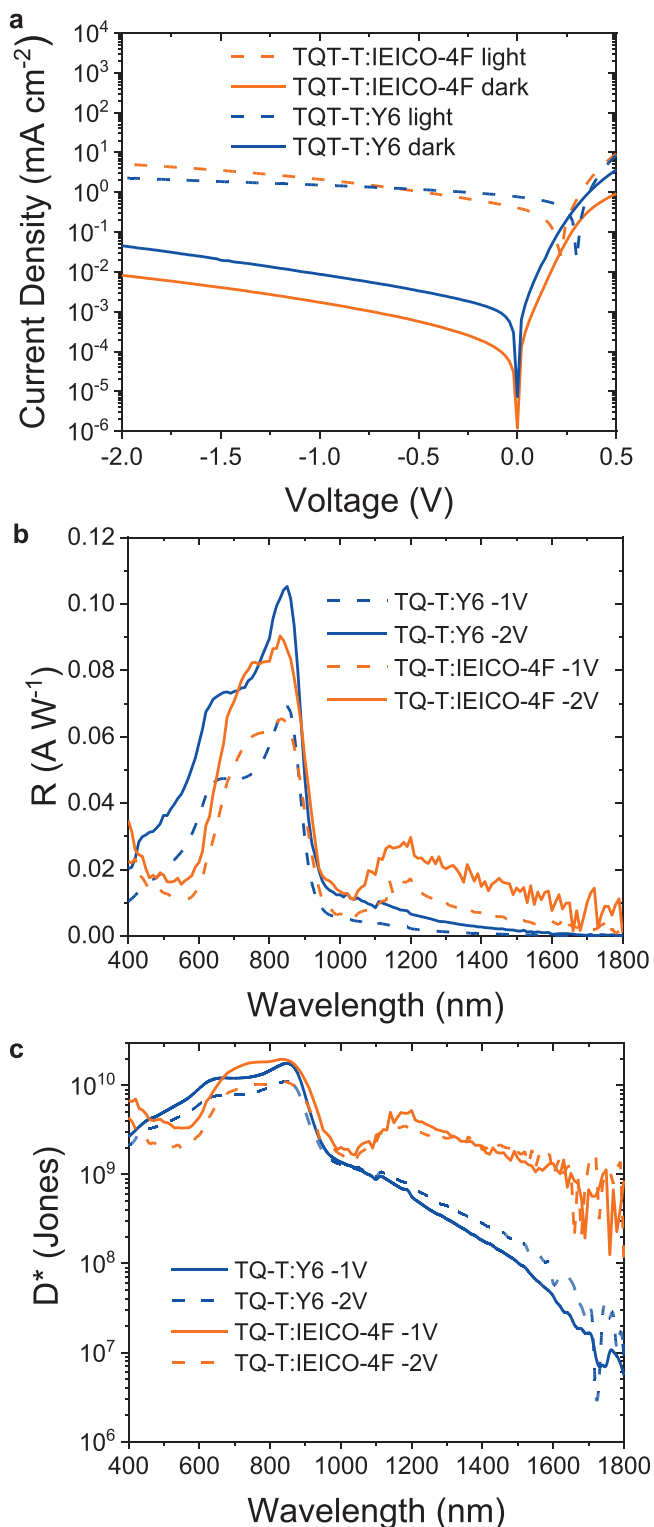
Figure 2. a) Current–voltage characteristics of TQ-T:IECO-4F and TQ-T:Y6 OPD devices under dark and AM1.5G illumination. b) Responsivity and c) specific detectivity of OPD devices under negative bias applied.

agreement with the superior OPD metrics of TQ-T:IEICO-4F reported above. In line with the superior light-harvesting capability of IEICO-4F-based devices, the illumination of OPD

devices with infrared light (940 nm) results in a similar LDR of 43.9 dB with AM1.5G illumination, while for TQ-T:Y6 devices the LDR in the infrared drop to 14.2 dB (Figure 3b). At 1100 nm illumination, TQ-T:Y6 devices did not allow any dynamic range, in line with the poor R values in the infrared region, together with the high J_d of the devices (Figure 3c), whereas TQ-T:IEICO-4F delivered an LDR value of 10.3 dB.

The cut-off frequency of OPDs is defined as the photoresponse drop of $1/\sqrt{2}$ of the maximum photocurrent intensity, known as −3 dB limit and calculated according to Equation (3), where i_{max} is the maximum photocurrent intensity and i_{freq} is the photocurrent intensity for a specific frequency of incident light.

$$Damping\,(dB) = -20log\left(\frac{i_{max}}{i_{freq}}\right) \qquad (3)$$

It is generally accepted that for video applications a cut-off frequency of 10 kHz is sufficient.[44] As shown in Figure 3c, both devices show fast response speeds, with values of 90 and 100 kHz for TQ-T:Y6 and TQ-T:IEICO-4F OPDs, respectively, and therefore fulfil the requirement for video applications. The faster response for IEICO-4F-based blends can be related to the reduced charge recombination and better charge extraction properties. To prove that, we studied the rise and fall times of OPDs by illuminating the devices with a square-wave pulse of 940 nm laser diode. Figure 3d shows the rise time for the two OPDs at an applied bias of −2 V. Notably, TQ-T:IEICO-4F depicts a faster rise time of 6.6 µs compared with 7.2 µs for the TQ-T:Y6 devices. The fall times are also showing the same trend and are 7.3 and 8.3 µs for TQ-T:IEICO-4F and TQ-T:Y6 OPDs, respectively. The transients measurements show that the superior performances of TQ-T:IEICO-4F are related to reduced charge recombination and improved transport properties compared to TQ-T:Y6 devices.

So far, we have investigated µs–ms charge transport and extraction processes in TQ-T-based devices. To find the origin of different spectral responsivity of two blends, we conducted transient absorption spectroscopy (TAS) to address the early stages of photon-to-charge conversion.

Given the energetics of these two systems and the ultranarrow bandgap of the polymer, we expect the polymer singlet exciton energy to be $E_{exciton} = 0.65$ eV and the charge transfer states (CT) emerging from donor excitation to be $E_{CT} = 0.51$ eV. As such, we were not able to observe these species using the infrared broadband probe, which tails off at 1600 nm. Therefore, we turned to a visible broadband probe to investigate the exciton/charge dynamics of the pristine materials and the two blends. **Figure 4** depicts the transient spectra of the two blends TQ-T:IEICO-4F and TQ-T:Y6, following the selective excitation of the TQ-T polymer with an infrared pump at 1500 nm. In Figure 4a,c, broad photoinduced absorption peaks are observed around 530 and 630 nm in both IEICO-4F and Y6 blends and are assigned to the donor exciton, according to the reference spectra of the neat donor and acceptor materials (Figures S8–S10, Supporting Information). Both blends also exhibit a bleach feature ≈750 and 730 nm for IEICO-4F and Y6 blends, respectively, which are assigned to the acceptor molecules in accordance with the transient and steady-state absorption spectra of
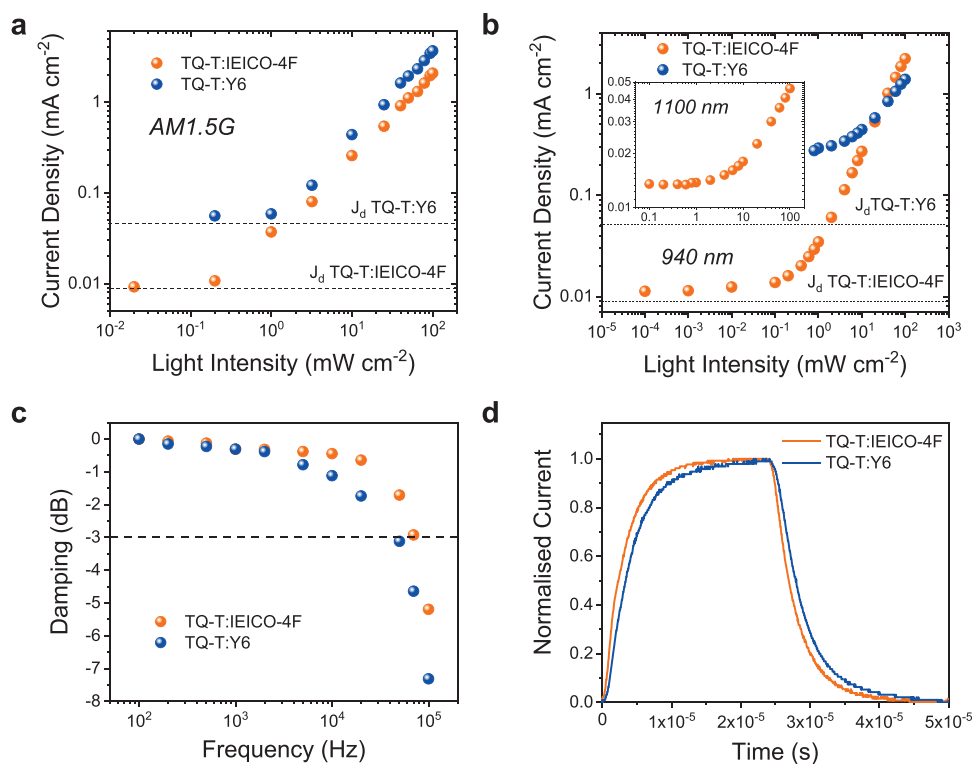
Figure 3. a) Light dynamic range at −2 V for TQ-T:IEICO-4F and TQ-T:Y6 under AM1.5G and b) IR illumination. c) Cut-off frequency and d) transient photocurrent measurements at −2 V for TQ-T-based OPD.

IEICO-4F and Y6. We assign these features to the ground state bleach (GSB) of the acceptors, which may be a consequence of the exciton or electron residing on the IEICO-4F/Y6 small molecules. For both blends, normalized kinetics of the shaded regions were averaged to maximize the signal to noise ratio and presented in Figure 4b,d. It is apparent from the shaded
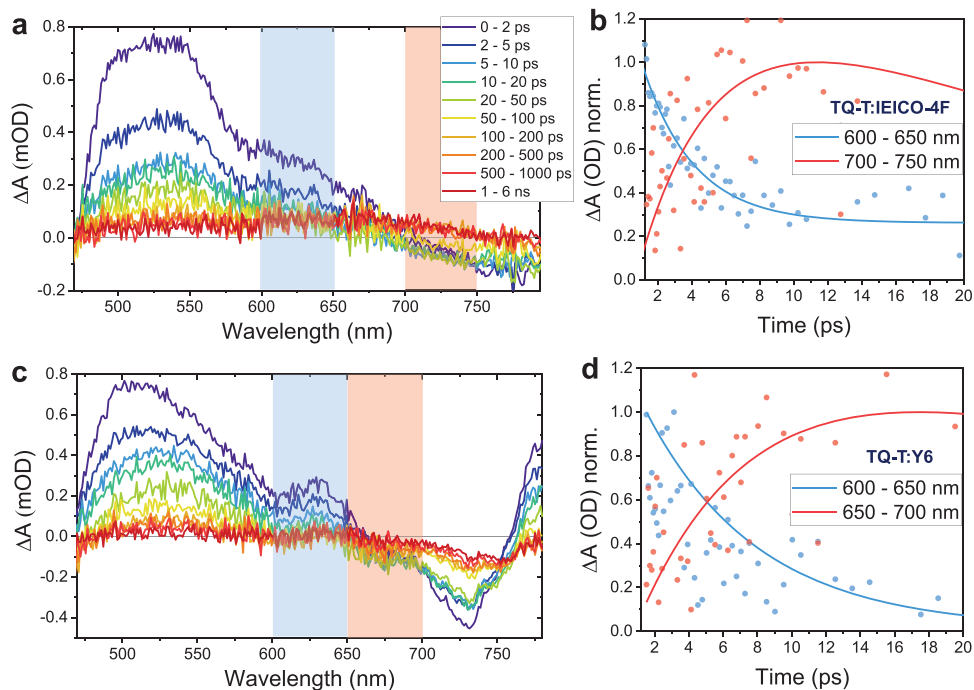

Figure 4. a) Transient absorption spectra of the TQ-T:IEICO-4F and c) TQ-T:Y6 blends at various pump-probe delay times and corresponding normalized kinetics (b, d) following the selective donor polymer excitation with a 1500 nm pump at 2 µJ cm^{-2}.
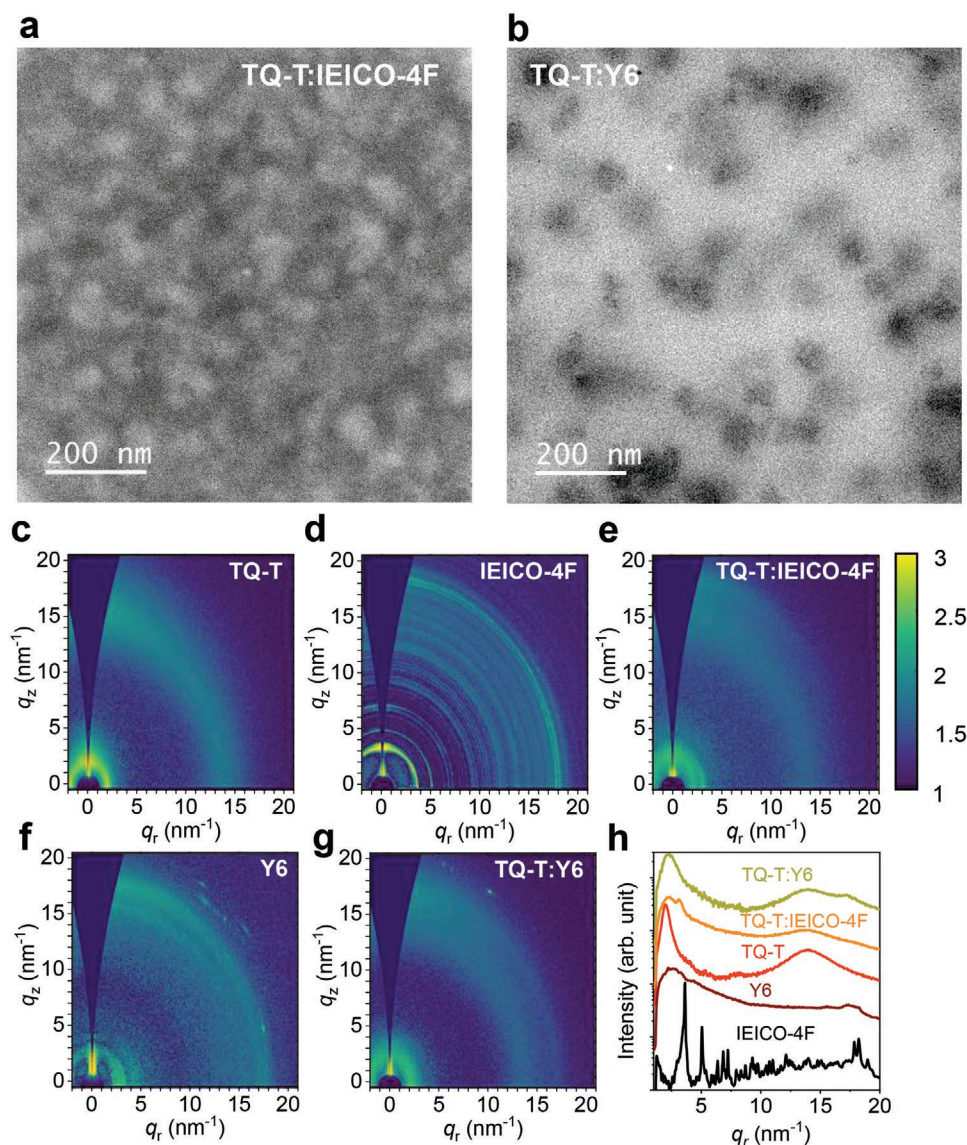
2200580 (5 of 10)

Figure 5. TEM images of a) TQ-T:IEICO-4F and b) TQ-T:Y6 blends. 2D GIWAXS patterns of c) TQ-T, d) IEICO-4F, e) TQ-T:IEICO-4F, f) Y6, and g) TQ-T:Y6. h) In-plane scattering profiles integrated from the 2D-GIWAXS patterns.

regions in the spectra that the temporal evolution of the TA signals differs for the photoinduced absorption exciton features around 630 nm and the negative signal at 725 nm for IEICO-4F blend and 675 nm for Y6 blend. Both negative signals exhibit a growth, which is attributed to charge carrier formation. Kinetic fitting at these wavelengths revealed lifetimes of 3 ps for TQ-T:IEICO-4F blend and 7 ps for TQ-T:Y6 blend. Although faster electron transfer may be expected in the TQ-T:IEICO-4F blend due to a larger energetic offset in the LUMO levels compared to the Y6 blend, low driving energy in polymer-NFA systems has been shown to not limit intrinsic charge transfer rates, that remain within hundred femtoseconds.[45]

To investigate whether the differences in device performance and photophysical processes have a microstructural origin, we performed transmission electron microscopy (TEM) investigations of the active layer films. **Figure 5**a,b shows the TEM bright-field images of TQ-T:IEICO-4F and TQ-T:Y6 blends,

respectively. Due to the similar carbon content in donor and acceptor materials is not possible to discern the two components from the images; however, it is clear that TQ-T:IEICO-4F depicts a finer morphology than TQ-T:Y6. A good intermixing of donor-acceptor materials generally leads to efficient exciton separation, whereas large D-A domains are associated with high exciton recombination.[46] The better intermixing of TQ-T:IEICO-4F compared to TQ-T:Y6 is also evident in the topography images obtained from atomic force microscopy (AFM) depicted in Figure S11a,b (Supporting Information). In addition, we calculated a root mean square (RMS) of 0.58 and 8.02 nm for TQ-T:IEICO-4F and TQ-T:Y6, respectively, which corroborates with the reduced charge recombination of IEICO-4F-based OPDs. Therefore, in line with the TAS analyses and the OPD's figures of merit, the smaller domains observed in TQ-T:IEICO-4F are responsible for the superior performance of the devices. To further probe the structural properties of
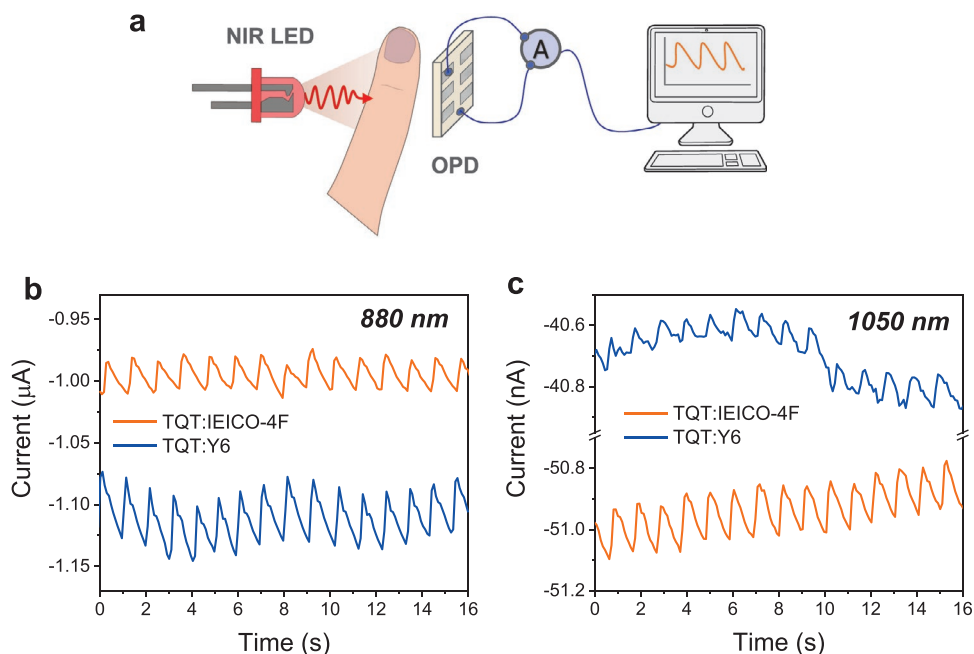
ADVANCED
SCIENCE NEWS
www.advancedsciencenews.com

NANO · MICRO
small
www.small-journal.com

Figure 6. a) Finger photoplethysmography setup with a direct current read-out; photoplethysmograms taken under normal (resting) conditions and ambient light using b) 880 nm and c) 1050 nm LEDs and OPDs.

our blend systems, we performed grazing-incidence wide-angle X-ray scattering (GIWAXS). Figure 5c–g shows the 2D GIWAXS patterns and the corresponding profiles along the in-plane direction (Figure 5h) for the neat materials and blends. While TQ-T and Y6 patterns show few and diffuse diffractions, suggesting the formation of a semi-crystalline microstructure with a low degree of structural order, IEICO-4F films exhibit high crystallinity, as it can be clearly deduced from their multiple, sharp diffractions. Such remarkable crystal quality is however considerably hampered when blended with TQ-T, despite a clear diffraction at low q, peaking around 3.1 nm^{-1}, associated with the NFA still clearly visible in the TQ-T:IEICO-4F blend, besides another diffraction at lower angles associated to the polymer. TQ-T:Y6 blends show GIWAXS patterns exhibiting a peak in the low-q-region, probably associated with diffractions from both TQ-T and Y6, besides broad peaks in the high-q-region. Hence, TQ-T:IEICO-4F and TQ-T:Y6 exhibit a rather similar microstructure.

Therefore, the observed 3 and 7 ps charge generation timescales from TAS can be attributed to morphological differences, rather than to changes in crystal quality between the two blends. The charge transfer in the TQ-T:Y6 blend is impeded by the large aggregate domains exceeding exciton diffusion length, while the TQ-T:IEICO-4F blend has smaller, more even domains, making it less susceptible to exciton recombination (**Figure 6**).

Finally, we demonstrate a practical application of the two NIR devices as biometric heart rate sensors using a technique known as photoplethysmography. This non-invasive optical technique typically comprises a light-emitting diode and an optoelectronic sensor, located on either side of a finger or another extremity. With blood pulsating through the capillaries, volumetric changes in the blood are detected as changes in

transmittance to the infrared light, and thereby as changes in photocurrent response of the OPD. By placing a finger between the OPD and NIR LED, the resting heart rate was measured using both TQ-T systems under 880 and 1050 nm illumination. Real-time current readouts for each device are presented. At 880 nm both OPD systems the two sensors performance is comparable and average ΔI ($I_{systolic} - I_{diastolic}$) is greater in the case of TQ-T:Y6, while the TQ-T:IEICO-4F device outperforms the TQ-T:Y6 one at 1050 nm (Table S1, Supporting Information). The signal resolution is significantly enhanced with TQ-T:IEICO-4F. This is unsurprising given the higher detectivity of this device beyond 1000 nm, which makes TQ-T:IEICO-4F a better candidate for IR detection with deeper tissue penetration.

Superior signal resolution is important not only for accurate heart rate evaluation, but also for potential uses as blood pressure monitors. For a given heart rate, the increasing amplitude of ΔI can act as a marker of elevated blood pressure on the capillaries. In addition, the HR before and after exercise was recorded using the 880 nm light and TQ-T:IEICO-4F device to reveal HR corresponding to 80 and 120 bpm (Figure S12, Supporting Information). In line with the high damping calculated for TQ-T-based OPDs, there is no limitation for the fast heart rate monitoring during strenuous exercise.

3. Conclusion

In conclusion, we fabricated organic photodetectors with UV–vis–NIR light-to-current conversion. Two novel blends comprising an ultralow bandgap polymer TQ-T and one of the two non-fullerene acceptors IEICO-4F or Y6 are reported. TQ-T:IEICO-4F featured a J_d of 8.4×10^{-3} mA cm^{-2} at -2 V and together with R of 0.03 A W^{-1} at 1200 nm delivered D^* of

**ADVANCED
SCIENCE NEWS**

www.advancedsciencenews.com

**NANO · MICRO
small**

www.small-journal.com

10^9–10^{10} Jones in the 350–1800 nm region. In contrast, TQ-T:Y6 showed lower J_d (4.3×10^{-2} mA cm^{-2}) and R of 0.01 A W^{-1} at 1200 nm, which results in D^* of 10^7–10^8 Jones across the NIR region (1000–1800 nm). The lower J_d in TQ-T:IEICO-4F extended the LDR to 46 and 44 dB compared to Y6-based devices (36 and 14 dB) under AM1.5G and IR illumination, respectively. We found that a finer intermixing of the TQ-T with IEICO-4F allows faster charge separation, rise and fall times as well as OPD response speed than in TQ-T:Y6 blends, the latter limited by severe phase segregation. Finally, we prototyped a biometric heart rate sensor based on the two OPDs and found enhanced signal resolution in TQ-T:IEICO-4F due to the higher D^* in the NIR region. Extending the light-to-current conversion beyond commercially viable Si-PD with NIR OPDs can propel the development of organic photodiodes not only for the Internet of Things market, but also contribute to health-monitoring.

4. Experimental Section

Materials: TQ-T was synthesized, details provided in the Supporting Information. The NFAs IEICO-4F and Y6 were purchased from 1-Material.

Photoelectron Spectroscopy in Air Measurements: PESA was recorded using a Riken Keiki PESA spectrometer (Model AC-2) with a power setting of 10 nW and a power number of 0.33. Samples for PESA were prepared on glass substrates.

Steady-State Absorption Spectroscopy: Absorption spectra were acquired on a Carry 5000 UV–vis–NIR spectrophotometer by Agilent Technologies.

Photodetector Fabrication: Organic photodiodes were fabricated in an inverted architecture of ITO/ZnO(30 nm)/Active Layer (120 nm)/MoO$_x$ (10 nm)/Ag(100 nm). Glass substrates pre-patterned with indium tin oxide (ITO) were cleaned by sequential sonication in acetone, deionised water, Decon 90 detergent, deionised water and propan-2-ol each for 10 min. Following this, an 8-min oxygen plasma treatment was performed. Zinc oxide (ZnO) precursor solution was prepared from zinc acetate dihydrate (219.5 mg), ethanolamine (60 μL), and 2-methoxyethanol (2 mL). This ZnO precursor solution was filtered through a 0.45 μm Acrodisc filter, spin-coated onto the plasma-treated substrates at 4000 rpm for 40 s, and annealed at 150 °C for 20 min. The TQ-T:Y6 (1:1) and TQ-T:IEICO-4F (1:1) were dissolved in chlorobenzene solution with a total concentration of 20 mg mL^{-1} and stirred overnight at 60 °C in a glove box. The active layers were deposited by spin coating at 2000 rpm for 40 s in inert conditions and then annealed at 100 °C for 10 min in the glove box. Molybdenum oxide (MoO$_x$) (10 nm) and silver (Ag) (100 nm) were then deposited by evaporation through a shadow mask giving photodiodes with pixel areas of 0.045 cm^2.

J–V Measurements: J–V characteristics were measured using Keithley 4200 Source-Measure unit. An Oriel Instruments Solar Simulator with a Xenon lamp and calibrated to a silicon reference cell was used to provide AM1.5G irradiance. For determination of the Linear Dynamic Range (LDR) this light was attenuated using a selection of neutral density filters placed between the lamp and OPD. For IR measurements 940 and 1100 nm LED were used. The photocurrent (J_{ph}) was calculated as the difference in response between the illuminated current density (J_{light}) and dark current density (J_d) at each light intensity.

Responsivity: Responsivity was measured using an integrated system from Quantum Design PV300. All the devices were tested in ambient air.

Dynamic Measurements: Dynamic measurements were performed using a digital oscilloscope (Siglent SDS 1204X-E). The OPDs were illuminated with a neutral white light LED driven by a function generator (ThorLabs DC2200). For determination of the rise and fall time, a 2 kHz square wave pulse was applied to the LED using the function generator. For determination of the cut-off frequency sinusoidal functions with varying frequencies between 20 Hz and 100 kHz were used to drive the LED.

Transient Absorption Spectroscopy: A broadband femtosecond transient absorption spectrometer Helios (Spectra-Physics, Newport Corp.) was used for pump-probe measurements on the neat polymer and acceptor films and their blends. A 1 kHz Ti:Sapphire regenerative amplifier (Solstice, Spectra-Physics, Newport Corp.) delivered ultrafast laser pulses (800 nm, <100 fs FWHM) to an optical parametric amplifier (TOPAS Prime, Spectra-Physics) and a frequency mixer (Niruvis, Light Conversion) to generate pump pulses at 850 and 1500 nm, which were modulated at 500 Hz by an optical chopper system (Thorlabs). Eight hundred nanometer seed pulses were also delayed on the 6 ns mechanical delay stage and passed through a sapphire crystal to produce a white light probe (400–900 nm). Spatial and temporal overlap of focused pump and probe beams was achieved on the thin film samples, contained in a quartz cuvette under a constant flow of nitrogen. The fluences were calculated based on the probe beam size of 0.5 mm^2 at the sample. Background and chirp corrections were applied to the spectra post-measurement using the Surface Xplorer software.

Photoplethysmography: Photoplethysmography measurements (Figure S13, Supporting Information) were performed by directly connecting the OPD devices to a Keithley 4200 Source-Measure unit and recording the current as a function of time upon illumination with different LEDs driven by a function generator (ThorLabs DC2200).

Grazing Incidence Wide Angle Scattering Measurements: Grazing incidence wide angle scattering (GIWAXS) measurements were performed at the non-crystalline diffraction beamline (BL11-NCD-Sweet) at ALBA Synchrotron Radiation Facility in Barcelona (Spain). A detector (Rayonix, WAXS LX255-HS) with a resolution of 1920 × 5760 pixels was used to collect the scattering signals. The sample holder position was calibrated with the chromium oxide (Cr$_2$O$_3$) standard. The incident energy was 12.4 eV and the sample-to-detector distance was set at 200.93 mm. The angle of incidence α$_i$ was set between 0.1 and 0.15 and the exposure time was 5 s. 2D-GIWAXS patterns were corrected as a function of the components of the scattering vector with a Matlab script developed by Aurora Nogales and Edgar Gutiérrez. Thin films were cast onto highly doped silicon substrates following the same processing route used for the device fabrication.

Transmission Electron Microscopy: The active layers for the TEM investigations were prepared as plan-view specimens. For this purpose, active-layer films were deposited on PEDOT:PSS (50–100 nm) coated glass using spin-coating. To float off the active layer, the sample was put into a vessel with distilled water, where PEDOT:PSS dissolved, and the active layer was transferred to a Cu TEM supporting grid. The TEM investigations were performed using an FEI instrument at 300 kV accelerating voltage.

Atomic Force Microscopy: AFM images were obtained with an Agilent AFM 5500 setup in tapping mode using Tap300Al-G silicon AFM probes from BudgetSensors and were processed with the PicoView 1.5 software.

Supporting Information

Supporting Information is available from the Wiley Online Library or from the author.

Acknowledgements

[1] Z. Wu, Y. Zhai, H. Kim, J. D. Azoulay, T. N. Ng, *Acc. Chem. Res.* **2018**, *51*, 3144.

[2] M. Babics, H. Bristow, W. Zhang, A. Wadsworth, M. Neophytou, N. Gasparini, I. McCulloch, *J. Mater. Chem. C* **2021**, *9*, 2375.

[3] M. Moser, A. Wadsworth, N. Gasparini, I. McCulloch, *Adv. Energy Mater.* **2021**, *11*, 2100056.

[4] F. P. Garcia de Arquer, A. Armin, P. Meredith, E. H. Sargent, *Nat. Rev.* **2017**, *2*, 1.

[5] S. E. Root, S. Savagatrup, A. D. Printz, D. Rodriquez, D. J. Lipomi, **2017**, https://doi.org/10.1021/acs.chemrev.7b00003.

[6] C. Fuentes-Hernandez, W.-F. Chou, T. M. Khan, L. Diniz, J. Lukens, F. A. Larrain, V. A. Rodriguez-Toro, B. Kippelen, *Science(80-)* **2020**, *370*, 698.

[7] S. Xing, V. C. Nikolis, J. Kublitski, E. Guo, X. Jia, Y. Wang, D. Spoltore, K. Vandewal, H. Kleemann, J. Benduhn, K. Leo, *Adv. Mater.* **2021**, *33*, 2102967.

[8] L. A. Sordillo, Y. Pu, S. Pratavieira, Y. Budansky, R. R. Alfano, *J. Biomed. Opt.* **2014**, *19*, 056004.

[9] E. Hemmer, A. Benayas, F. Légaré, F. Vetrone, *Nanoscale Horiz.* **2016**, *1*, 168.

[10] S. Wang, J. Y. Oh, J. Xu, H. Tran, Z. Bao, *Acc. Chem. Res.* **2018**, *51*, 1033.

[11] S. Inal, J. Rivnay, A. O. Suiu, G. G. Malliaras, I. McCulloch, *Acc. Chem. Res.* **2018**, *51*, 1368.

[12] Y. H. Lee, O. Y. Kweon, H. Kim, J. H. Yoo, S. G. Han, J. H. Oh, *J. Mater. Chem. C* **2018**, *6*, 8569.

[13] N. Li, Z. Lan, Y. S. Lau, J. Xie, D. Zhao, F. Zhu, *Adv. Sci.* **2020**, *7*, 2000444.

[14] J. Huang, J. Lee, J. Vollbrecht, V. V. Brus, A. L. Dixon, D. Xi Cao, Z. Zhu, Z. Du, H. Wang, K. Cho, G. C. Bazan, T.-Q. Nguyen, J. Huang, J. Lee, J. Vollbrecht, V. V. Brus, A. L. Dixon, D. X. Cao, Z. Zhu, Z. Du, G. C. Bazan, T. Nguyen, H. Wang, K. Cho, *Adv. Mater* **2020**, *32*, 1906027.

[15] N. Gasparini, M. Salvador, S. Strohm, T. Heumueller, I. Levchuk, A. Wadsworth, J. H. Bannock, J. C. de Mello, H.-J. Egelhaaf, D. Baran, I. McCulloch, C. J. Brabec, *Adv. Energy Mater.* **2017**, *7*, 1700770.

[16] N. Gasparini, A. Gregori, M. Salvador, M. Biele, A. Wadsworth, S. Tedde, D. Baran, I. McCulloch, C. J. Brabec, *Adv. Mater. Technol.* **2018**, *3*, 1800104.

[17] G. Li, W.-H. Chang, Y. Yang, *Nat. Rev. Mater.* **2017**, *2*, 17043.

[18] C. J. Traverse, R. Pandey, M. C. Barr, R. R. Lunt, *Nat. Energy* **2017**, *2*, 849.

[19] A. Wadsworth, Z. Hamid, J. Kosco, N. Gasparini, I. McCulloch, *Adv. Mater.* **2020**, *32*, 2001763.

[20] Z. Zhao, M. Liu, K. Yang, C. Xu, Y. Guan, X. Ma, J. Wang, F. Zhang, *Adv. Funct. Mater.* **2021**, *31*, 2106009.

[21] M. Liu, J. Wang, K. Yang, Z. Zhao, Z. Zhou, Y. Ma, L. Shen, X. Ma, F. Zhang, *J. Mater. Chem. C* **2021**, *9*, 6357.

[22] J. Lee, S.-J. Ko, H. Lee, J. Huang, Z. Zhu, M. Seifrid, J. Vollbrecht, V. V. Brus, A. Karki, H. Wang, K. Cho, T.-Q. Nguyen, G. C. Bazan, *ACS Energy Lett.* **2019**, 1401.

[23] Y. J. Cheng, S. H. Yang, C. S. Hsu, *Chem. Rev.* **2009**, *109*, 5868.

[24] Z. H. Zhou, T. Maruyama, T. Kanbara, T. Ikeda, K. Ichimura, T. Yamamoto, K. Tokuda, *J. Chem. Soc., Chem. Commun.* **1991**, 1210.

[25] L. Dou, Y. Liu, Z. Hong, G. Li, Y. Yang, *Chem. Rev.* **2015**, *115*, 12633.

[26] E. Perzon, F. Zhang, M. Andersson, W. Mammo, O. Inganäs, M. R. Andersson, *Adv. Mater.* **2007**, *19*, 3308.

[27] F.-J. Kahle, A. Rudnick, H. Bässler, A. Köhler, *Mater. Horiz* **2018**, *5*, 837.

[28] A. Wadsworth, M. Moser, A. Marks, M. S. Little, N. Gasparini, C. J. Brabec, D. Baran, I. McCulloch, *Chem. Soc. Rev.* **2019**, *48*, 1596.

[29] P. Meredith, W. Li, A. Armin, *Adv. Energy Mater.* **2020**, *10*, 2001788.

[30] N. Gasparini, F. V. A. Camargo, S. Frühwald, T. Nagahara, A. Classen, S. Roland, A. Wadsworth, V. G. Gregoriou, C. L. Chochos, D. Neher, M. Salvador, D. Baran, I. McCulloch, A. Görling, L. Lüer, G. Cerullo, C. J. Brabec, *Nat. Commun.* **2021**, *12*, 1772.

[31] D. Baran, T. Kirchartz, S. Wheeler, S. Dimitrov, M. Abdelsamie, J. Gorman, R. S. Ashraf, S. Holliday, A. Wadsworth, N. Gasparini, P. Kaienburg, H. Yan, A. Amassian, C. J. Brabec, J. R. Durrant, I. McCulloch, *Energy Environ. Sci.* **2016**, *9*, https://doi.org/10.1039/c6ee02598f.

[32] T. Zhang, M. Moser, A. D. Scaccabarozzi, H. Bristow, P. Jacoutot, A. Wadsworth, T. D. Anthopoulos, I. McCulloch, N. Gasparini, *J. Phys. Mater.* **2021**, *4*, 045001.

[33] A. Armin, R. D. Jansen-Van Vuuren, N. Kopidakis, P. L. Burn, P. Meredith, *Nat. Commun.* **2015**, *6*, 6343.

[34] C. M. Yang, P. Y. Tsai, S. F. Horng, K. C. Lee, S. R. Tzeng, H. F. Meng, J. T. Shy, C. F. Shu, *Appl. Phys. Lett.* **2008**, *92*, 7.

[35] Z. Tang, Z. Ma, A. Sánchez-Díaz, S. Ullbrich, Y. Liu, B. Siegmund, A. Mischok, K. Leo, M. Campoy-Quiles, W. Li, K. Vandewal, *Adv. Mater* **2017**, *29*, 1702184.

[36] B. Siegmund, A. Mischok, J. Benduhn, O. Zeika, S. Ullbrich, F. Nehm, M. Böhm, D. Spoltore, H. Fröb, C. Körner, K. Leo, K. Vandewal, *Nat. Commun.* **2017**, *8*, 15421.

[37] J. Kublitski, A. Hofacker, B. K. Boroujeni, J. Benduhn, V. C. Nikolis, C. Kaiser, D. Spoltore, H. Kleemann, A. Fischer, F. Ellinger, K. Vandewal, K. Leo, *Nat. Commun.* **2021**, *12*, 551.

[38] H. Bristow, P. Jacoutot, A. D. Scaccabarozzi, M. Babics, M. Moser, A. Wadsworth, T. D. Anthopoulos, A. Bakulin, I. McCulloch, N. Gasparini, *ACS Appl. Mater. Interfaces* **2020**, *12*, 48836.

[39] S. Gielen, C. Kaiser, F. Verstraeten, J. Kublitski, J. Benduhn, D. Spoltore, P. Verstappen, W. Maes, P. Meredith, A. Armin, K. Vandewal, *Adv. Mater.* **2020**, *32*, 2003818.

[40] T. T. Steckler, P. Henriksson, S. Mollinger, A. Lundin, A. Salleo, M. R. Andersson, *J. Am. Chem. Soc* **2014**, *136*, 1190.

[41] W. Zhao, S. Li, H. Yao, S. Zhang, Y. Zhang, B. Yang, J. Hou, *J. Am. Chem. Soc.* **2017**, *139*, 7148.

[42] J. Yuan, Y. Zhang, L. Zhou, G. Zhang, H. Yip, T. Lau, X. Lu, C. Zhu, H. Peng, P. A. Johnson, M. Leclerc, Y. Cao, J. Ulanski, Y. Li, Y. Zou, *Joule* **2019**, *3*, 1140.

2200580 (9 of 10)

[43] Y. Fang, A. Armin, P. Meredith, J. Huang, *Nat. Photonics* **2019**, *13*, 1.

[44] R. D. Jansen-van Vuuren, A. Armin, A. K. Pandey, P. L. Burn, P. Meredith, *Adv. Mater.* **2016**, *28*, 4766.

[45] Y. Zhong, M. Causa, G. J. Moore, P. Krauspe, B. Xiao, F. Günther, J. Kublitski, R. Shivhare, J. Benduhn, E. BarOr, S. Mukherjee, K. M. Yallum, J. Réhault, S. C. B. Mannsfeld, D. Neher, L. J. Richter, D. M. DeLongchamp, F. Ortmann, K. Vandewal, E. Zhou, N. Banerji, *Nat. Commun.* **2020**, *11*, 833.

[46] N. Gasparini, M. Salvador, S. Fladischer, A. Katsouras, A. Avgeropoulos, E. Spiecker, C. L. Chochos, C. J. Brabec, T. Ameri, *Adv. Energy Mater.* **2015**, *5*, 1501527.